Evidence of exchange striction and charge disproportionation in the magnetoelectric material Ni_3TeO_6

Mohamad Numan,[1] Gangadhar Das,[2] Md Salman Khan,[3,*] Gouranga Manna,[4] Anupam Banerjee,[1] Saurav Giri,[1] Giuliana Aquilanti,[2] and Subham Majumdar[1,†]

[1]*School of Physical Sciences, Indian Association for the Cultivation of Science, 2A & B Raja S. C. Mullick Road, Jadavpur, Kolkata 700 032, India*

[2]*Elettra Sincrotrone Trieste, Strada Statale 14, km 163.5 in AREA Science Park, Basovizza, Trieste 34149, Italy*

[3]*School of Materials Sciences, Indian Association for the Cultivation of Science, 2A & B Raja S. C. Mullick Road, Jadavpur, Kolkata 700 032, India*

[4]*New Chemistry Unit, Jawaharlal Nehru Centre For Advanced Scientific Research, Rachenahalli Lake Rd, Jakkur, Bengaluru, Karnataka 560064, India*

(Received 7 September 2022; revised 8 December 2022; accepted 9 December 2022; published 27 December 2022)

The chiral magnetoelectric compound Ni_3TeO_6 is investigated through temperature-dependent synchrotron-based powder x-ray diffraction and x-ray absorption spectroscopy between 15 and 300 K. Our work provides direct evidence for the exchange-striction in the material around the concomitant onset point of collinear antiferromagnetic and the magnetoelectric phases. The x-ray absorption near edge spectra and x-ray photoelectron spectra show that the sample consists of both Ni^{2+} and Ni^{3+} ions in the lattice. The ionic state of Ni is found to be quite robust, and it is largely independent of the preparation route. Additionally, a minority Te^{4+} state is found to coexist with the majority Te^{6+} state, which may arise from the charge disproportionation between Ni and Te ions ($Ni^{2+} + Te^{6+} \Longleftrightarrow Ni^{3+} + Te^{4+}$). The observed mixed valency of Ni is also confirmed by the total paramagnetic moment (μ_{eff}) per Ni atom in the system. This mixed valency in the metal ions and the exchange-striction may be attributed to the observed magnetoelectric effect in the system.

DOI: 10.1103/PhysRevB.106.214437

I. INTRODUCTION

The intriguing coupling between magnetic and electric orders in solid leads to the fascinating phenomenon of multiferroicity [1–4]. Type-II multiferroics are found to have large magnetoelectric (ME) coupling [5]. They often show large ME effect [6–8], where the electric polarization can be altered by the magnetic field and vice versa. Type-II multiferroicity in a solid can originate from different underlying mechanisms, such as (i) inverse Dzyaloshinskii-Moriya interaction via antisymmetric spin-exchange interaction (spin current mechanism) [9,10]; (ii) symmetric spin exchange interaction in collinear magnets (Heisenberg exchange striction) [11]; and (iii) *p-d* hybridization between the metal and the ligand [12–14]. In certain cases, more than one mechanism can be present for multiferroicity [15].

In recent times, several 3*d* transition metal tellurates (M_3TeO_6, M = Mn, Co, Ni, Cu) having Corundum-type structure are found to be relevant materials for multiferroicity. These compounds crystallize with a chiral structure (space group *R*3), which lacks both mirror and inversion symmetry. The interest in these Corundum materials is renewed after the discovery of extremely large ME effect in Ni_3TeO_6 (NTO) [16]. The compound orders antiferromagnetically below T_N = 52 K with a collinear structure [17]. NTO shows metamagnetic transition under $H = 86$ kOe at 2 K from a collinear antiferromagnetic to a incommensurate spiral structure [18]. Although, it does not show spontaneous electric polarization (P) below T_N under zero magnetic field ($H = 0$), a large ME effect is observed below T_N under the application of H and P attains a value of 3280 $\mu C/m^2$ at 2 K for an applied field of 90 kOe (P, $H \parallel c$) [16]. Despite the colossal ME effect is observed beyond the metamagnetic transition at 86 kOe, a significant field-induced polarization is present even at lower fields [19,20].

In NTO, Ni cations occupy three different Wyckoff 3*a* sites [Ni(1), Ni(2), and Ni(3)], whereas Te cations reside only on a single Wyckoff 3*a* site(see Table I). Three NiO_6 octahedra [see Fig. 1(b)] and the TeO_6 octahedron are found to be face sharing, edge sharing, and corner sharing among each other [17]. Along the *c* axis, there are two different pairs of face-shared octahedra, one is between $Ni(2)O_6$ and $Ni(3)O_6$ and the other is between $Ni(1)O_6$ and TeO_6. In the *ab* plane, there are two different pairs of corner sharing octahedra [$Ni(1)O_6$-$Ni(2)O_6$ and $Ni(3)O_6$-TeO_6]. These corner sharing octahedra form a honeycomb-like structure in the *ab* plane with a slight offset in the *c* axis.

It has been mooted that symmetric exchange-striction can be the possible reason for the ME effect, particularly in the low-field region [16]. Exchange striction occurs due to the competition between lattice and magnetic energies in the

*Present address: Department of Energy Science, Sungkyunkwan University, Suwon 16419, Republic of Korea.

†sspsm2@iacs.res.in

TABLE I. Refined coordinates and reliability parameters with *R*3 space group at selective temperatures in between 15 K and 300 K.

	Ni(1)			Ni(2)			Ni(3)			Te			Reliability parameters		
T(K)	*x*	*y*	*z*	*x*	*y*	*z*	*x*	*y*	*z*	*x*	*y*	*z*	$R_{wp}(\%)$	$R_{exp}(\%)$	χ^2
300	1/3	2/3	0.1789(3)	0	0	0.2092(5)	2/3	1/3	0.3451(5)	1/3	2/3	0.3817(2)	10.96	5.86	1.87
150	1/3	2/3	0.1884(5)	0	0	0.2117(7)	2/3	1/3	0.3492(7)	1/3	2/3	0.3821(2)	10.63	5.81	1.83
60	1/3	2/3	0.2150(5)	0	0	0.2511(3)	2/3	1/3	0.3874(6)	1/3	2/3	0.4175(9)	9.64	5.60	1.72
15	1/3	2/3	0.1681(4)	0	0	0.2081(0)	2/3	1/3	0.3421(1)	1/3	2/3	0.3710(3)	7.12	4.24	1.68

system. When the system undergoes long-range magnetic ordering, the magnetic ions may slightly relocate their position to compensate the additional magnetic energy [21]. Despite the above conjecture of exchange striction, there is hardly any work available in the literature for its experimental verification. We addressed this problem from the structural point of view using both x-ray diffraction and the x-ray absorption spectroscopy tools. The temperature (T) dependent powder x-ray diffraction (PXRD) shows a clear anomaly in the lattice parameters of NTO around T_N. The x-ray absorption spectroscopy also indicates a noticeable change in the bond length between the metal ion and oxygen (Ni-O) inside the NiO_6 octahedra close to T_N. The exchange striction is also indirectly evident from the change in the pre-edge peak area with T as well as the presence of thermal hysteresis in the magnetization versus temperature data. The thermal hysteresis indicates that the magnetic transition is first order in nature. The charge state of Ni was earlier assumed to be +2. However, our investigation of the near edge x-ray absorption spectra (XAS) data indicates that there is a charge disproportionation between Ni and Te sites resulting in both Ni^{2+} and Ni^{3+} ions.

II. EXPERIMENTAL METHODS

A polycrystalline sample of Ni_3TeO_6 was prepared by standard solid-state reaction method using high purity (>99.99%) starting materials. The stoichiometric amount of NiO and TeO_2 were ground and mixed thoroughly, and heated at 750° C for 15 hours. It was then pressed into a pellet and heated at 800° C for 24 hours. The final heat treatment was done at 830° C [22,23] in air. In addition to this air-annealed sample (NTO-air), we also prepared samples which are annealed in a vacuum (NTO-vac) and oxygen flow (NTO-oxy) [24]. Primary measurements were performed on NTO-air, while NTO-vac and NTO-oxy were also investigated to confirm the charge state of Ni through magnetic measurements and photoelectron spectroscopy. The phase purity of the samples was determined using RIGAKU Smartlab (9 KW) XG equipped with Cu K_α (wavelength, $\lambda = 1.5406$ Å). Beside that, all the temperature-dependent (15–300 K) x-ray diffraction (XRD) patterns were obtained using high-flux synchrotron radiation source (energy = 10 keV) at the Indian Beamline, BL-18B, Photon Factory, Japan. The powder XRD

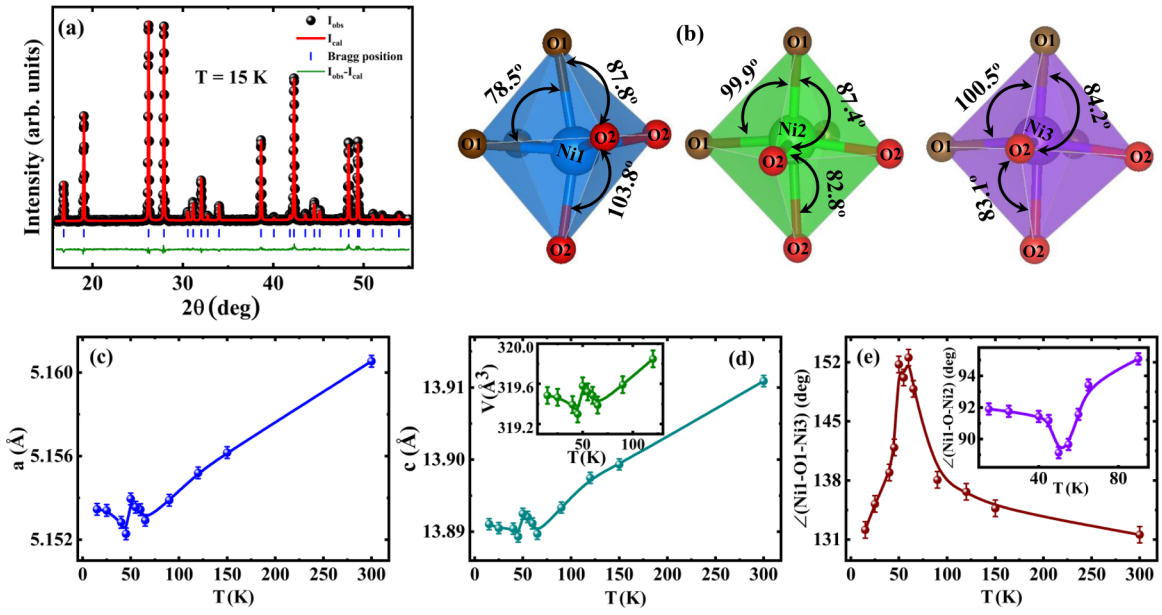

FIG. 1. (a) The synchrotron (energy = 10 keV) x-ray diffraction pattern recorded on NTO-air at 15 K along refinement. (b) The different bond angle between O-Ni-O inside three different NiO_6 octahedra at three different Ni sites at 15 K. (c), (d) The thermal variation of lattice parameters (a and c), respectively. (e) Illustrates the temperature variation of $\angle$[Ni(1) − O1 − Ni(3)] bond angle, which is associated with the highest magnitude of magnetic exchange interaction path. The insets in (d,e) show the temperature variation of the lattice volume and the bond angle $\angle$[Ni(1) − O − Ni(2)] averaged over two oxygen sites, respectively.

patterns were analyzed using Rietveld technique and the refinement of the crystalline parameter was obtained by using the MAUD software package [25]. This confirms that all the samples of Ni_3TeO_6 are single phase and crystallizes in the corundum $R3$ space group at room temperature. The magnetization (M) of the samples was measured using the vibrating sample magnetometer (VSM) module of the Quantum Design physical properties measurement system (Dynacool model) as well as Quantum Design superconducting quantum interference vibrating sample magnometer (SQUID-VSM) (MPMS3) in the temperature range 2–300 K. The temperature-dependent (20–300 K) x-ray absorption spectroscopy (XAS) measurements were performed at the Ni-K absorption edge at the XAFS Beamline of Elettra Sincrotrone Trieste, Italy [26]. We also recorded the room-temperature data at Te-L_3 edge spectra. The incident energy was selected using a Si(111) double crystal monochromator. The x-ray absorption near edge structure (XANES) and the extended x-ray absorption fine structure (EXAFS) parts of the acquired XAS data were processed and analyzed using the DEMETER open source package (ATHENA and ARTEMIS) [27,28]. The x-ray photoemission spectroscopy (XPS) was performed on a laboratory-based electron spectrometer (Omicron) using Al K_α monochromatic source, and a seven-channel Channeltron detector.

III. RESULTS

A. Powder x-ray diffraction

Rietveld refinement of the obtained PXRD patterns at 15 K is shown in Fig. 1(a), which confirms that the sample retains its room-temperature crystal symmetry at least down to 15 K. The refined coordinates for all the cations are shown in Table I, which shows nonmonotonic change in the position of all the cations close to 60 K. As already mentioned there are three different Ni sites and they form three different distorted NiO_6 octahedra. The schematic view of three such octahedra, as obtained from our PXRD data 15 K, are shown in Fig. 1(b). For an ideal octahedra, the Ni-O-Ni bond angle is 90° and one can see that the actual angles differ considerably from 90° in the NiO_6 octahedra. The distortion is trigonal type, where there is an elongation of the octahedra along the threefold symmetry axis [29–31].

The temperature variation of the lattice parameters (a and c) are shown in Figs. 1(c) and 1(d). Both a and c decrease with temperature monotonically down to 70 K. A clear anomaly in both the lattice parameters has an onset at 60 K and continues down to 40 K, which matches well with the magnetic transition temperature ($T_N \sim 54$ K) of the sample. This indicates that the system undergoes some structural changes, albeit the lattice symmetry remains the same. Previous density functional theory (DFT) calculation indicates that the strongest Ni-Ni interaction is antiferromagnetic (AFM) type and it occurs via O atom between Ni(1) and Ni(3) [32]. We plotted the temperature variation of the bond angle $\angle$[Ni(1) − O − Ni(3)] in Fig. 1(e). The data show a prominent peak at around T_N with the peak value of 152°. This value is closer to 180° required for the AFM superexchange in accordance with the Goodenough-Kanamori rule [33–35]. On the other hand, the bond angle associated with the strongest ferromagnetic (FM) interaction also shows an anomaly around T_N with its maximum value of 95° [see the inset of Fig. 1(e)], which is favorable for the FM interaction. The observed anomaly at around T_N indicates the presence of strong magnetostructural correlation in the system. It is to be noted that the previous works on the sample also hypothesised the role of the exchange striction towards the development of polarization below T_N [16].

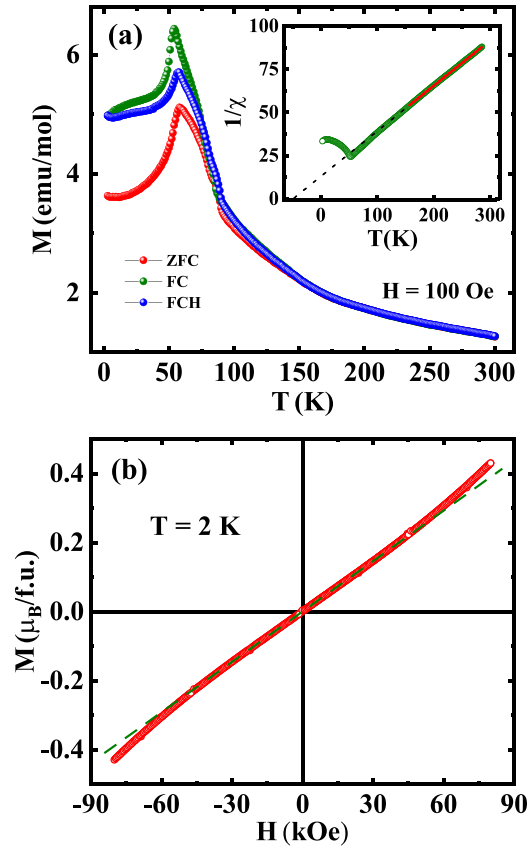

FIG. 2. (a) Field-cooling (FC), field-cooled-heating (FCH), and zero-field-cooled-heating (ZFC) magnetization as a function of temperature measured under 100 Oe of field for NTO-air. The inset shows the inverse magnetic susceptibility with a Curie-Weiss fit between 150–300 K having $\theta_p = -49$ K. (b) The isothermal magnetization curve at $T = 2$ K up to a field of ± 80 kOe. The dashed straight line is added to show the deviation from the straight line.

B. Magnetization

Figure 2 shows the magnetization as a function of temperature measured in the field-cooling (FC), field-cooled-heating (FCH), and zero-field-cooled-heating (ZFC) protocols under 100 Oe of applied field (H). An AFM-like transition is clearly visible at around $T_N = 54$ K, which match well with the previous reports [17]. The ZFC curve deviates from the FCH data below about 90 K. The FC and FCH data show clear thermal hysteresis over a wide temperature range (4–74 K), which also include the T_N. This indicates that the transition around T_N is first order in nature. The inverse susceptibility ($1/\chi = H/M$) is found to be linear above about 150 K, and a Curie-Weiss fit to the data (see the inset of Fig. 2) indicates

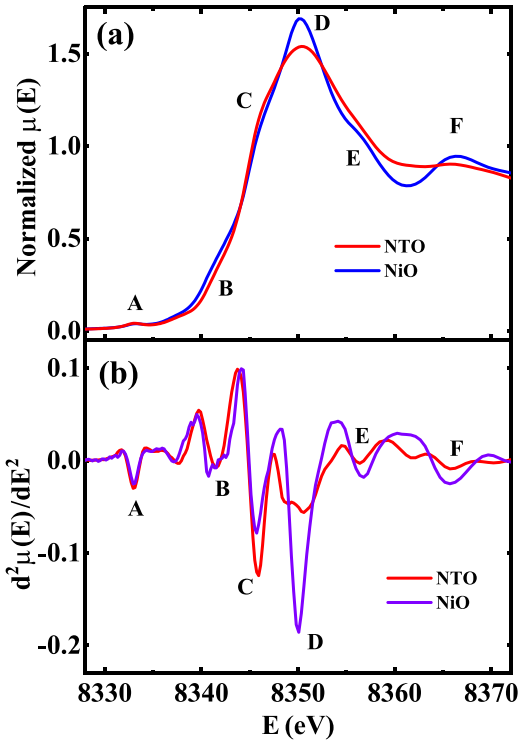

FIG. 3. (a) The normalized Ni-K absorption edge measured at 300 K for NTO-air and the standard NiO. (b) Second derivative of the normalized absorption coefficient (μ) as a function of incident energy.

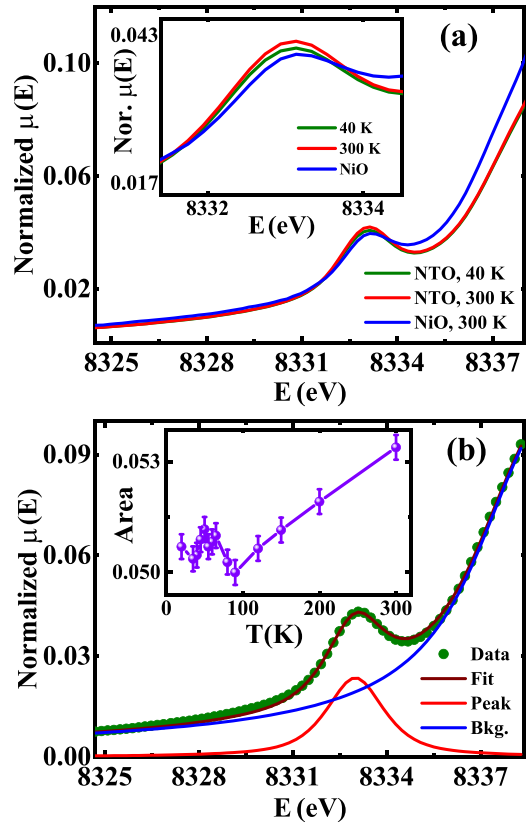

FIG. 4. (a) The normalized pre-edge of the Ni-K absorption data at 40 and 300 K for NTO-air. The NiO pre-edge is also shown for the comparison. The inset shows an enlarged view of the normalized pre-edge measured at both the temperatures. (b) The fitting of the 300 K pre-edge data using arc tangent function (blue line as background) and a pseudo-voigt function (red line). The inset shows the intensity (area under the curve) of the pre-edge with temperature.

that the effective moment $\mu_{\text{eff}} = 3.32 \pm 0.02\ \mu_B$/Ni and the paramagnetic Weiss temperature $\theta_p = -49$ K for NTO-air. For the Ni^{2+} state with spin $S = 1$, the expected spin-only moment is 2.83 μ_B. The higher value of the effective moment indicates either orbital contribution or due to a different charge state of Ni. The μ_{eff} values of NTO-vac and NTO-oxy are found to be 3.32 μ_B/Ni and 3.35 μ_B/Ni, respectively, indicating that the moment value of NTO does not depend upon the preparation condition. The isothermal magnetization versus field data is shown in Fig. 2(b). The curve is quasilinear in the low-field region (below 50 kOe) and a clear upward curvature is seen at higher applied field. One can relate this curvature to the metamagnetism observed in the sample reported earlier [19].

C. X-ray absorption near edge structure

To maintain the stoichiometric formula of Ni_3TeO_6, it is reasonable to assume that Ni and Te are in the 2+ and 6+ states, respectively. However, it is known that Ni and Te can assume multiple charge states which can create mixed valency at the Ni and Te sites. In addition, oxygen off-stoichiometry can also create mixed valency of the cations [36,37]. Such mixed valency can greatly alter the strength of the magnetic interactions between Ni ions.

1. Ni-K edge

To reaffirm the charge states of the cations, we analyzed the XANES spectra at the Ni-K edge as shown in Fig. 3. The obtained spectra were aligned using standard Ni metal foil data in the reference channel. The XANES spectra at the Ni-K edge shows few distinct features, which are designated as *A*–*F* in Fig. 3. These features originate from different kinds of electronic transitions from the 1*s* level to higher-energy states of the Ni atom in the distorted octahedral environment of oxygen. We also recorded the Ni-K edge spectra of NiO in the same set up along with the sample.

Pre-edge: A small hump like feature designated as *A* in Fig. 3(a) around 8333 eV is known as the pre-edge. This is a dipole forbidden transition from 1*s* to 3*d* electronic states of Ni, which is weakly allowed via quadrupole transition. A prominent pre-edge can occur due to the admixture of 3*d* level with 4*p* level of the metal provided the active metal site is in noncentrosymmetric environment [38,39]. A pre-edge region can also occur due to the dipole-allowed transition from 1*s* to the hybridized state of Ni-3*d* and O-2*p* levels.

We fit the pre-edge using the combination of an arc-tangent (background) and a pseudo-voigt (pre-edge peak) functions as illustrated in Fig. 4(b) for the 300-K data. The pseudo-voigt peak position is found to be at 8333 eV and this position is independent of temperature. The area under the pre-edge peak (pseudo-voigt) decreases almost linearly with decreasing temperature [see inset of Fig. 4(b)] down to about 80 K. Similar linear variation of the pre-edge peak area was ob-

TABLE II. Temperature variation of the area under the fitted (pseudo-voigt) curve of the pre-edge.

Sample	Temperature (K)	Area under the curve
	300	0.0528(9)
Ni_3TeO_6	120	0.0501(5)
	35	0.0498(7)
NiO	300	0.0407(2)

served in other transition metals and it is possibly related to the dynamic displacement of the absorbing atoms [40,41]. Interestingly, the area under pre-edge shows a nonmonotonic variation below 80 K. The pre-edge intensity shows a distinct peak, which matches well with the T_N of the sample. Notably, we find that the pre-edge peak area of NiO is about 23% less than that of the NTO at 300 K (see Table II).

Main absorption peak: The main absorption peak in the XANES spectra originates from the electronic transition from the occupied inner level to unoccupied outer levels. In this case, a dipole-allowed transition occurrs from $1s$ to $4p$ levels of Ni. Further increase in the x-ray energy leads to transition to the continuum. In Fig. 3(a), the XANES spectra of NTO along with NiO are plotted. The positions of the XANES rising line [region *B*–*D* in Fig. 3(a)] in NTO is shifted towards the higher energy as compared to NiO. The shift of the XANES rising line to higher energy with oxidation state is a common phenomenon. The effective attractive potential on the $1s$ core electrons by the nucleus increases with the increase in oxidation state of the cation. Because the repulsive Coulomb interaction between $1s$ and the other electrons decreases when the cation attains a higher valence state [42]. The first derivative of the absorption coefficients $[d\mu(E)/dE]$ for NTO at the onset of rising edge is found to shifted (~ 0.2 eV) towards higher energy than that of NiO. This also implies that Ni in NTO is not completely in the 2+ state and some fraction of Ni ions are in the higher oxidation state (Ni^{3+}).

The shift in the energy position is also clearly visible in the plot of the second derivatives of the absorption coefficient $[d^2\mu(E)/dE^2]$ [Fig. 3(b)]. It is to be noted that the nature of the plot is significantly different at the point *D* (main peak). $d^2\mu(E)/dE^2$ is quite sharp at *D* for NiO, while it is broad and split into two for NTO-air. Interestingly, for the Li-doped NiO samples, where Ni is mixed valent (2+ and 3+), identical feature in $d^2\mu(E)/dE^2$ is observed [43]. This also an another indication of the mixed valent state of NTO. Below the main peak, we observe few anomalies at the points *B* and *C*, which are also reflected in the $d^2\mu(E)/dE^2$ plot. Such features are often observed in the XANES data of metal oxides, and generally attributed to the charge transfer from metal to ligand [44].

2. Te-L_3 edge

We also recorded the spectra of the Te-L_3 edge as shown in Fig. 5 along with the standard samples of TeO_2 (Te in 4+) and TeO_3 (Te in 6+). Evidently, the L_3 rising edge of NTO lies between that of TeO_2 and TeO_3, although it is closer to the TeO_3 sample [45–47]. The rising edge of NTO shows a characteristic peak at 4357 eV whereas for TeO_2 and TeO_3,

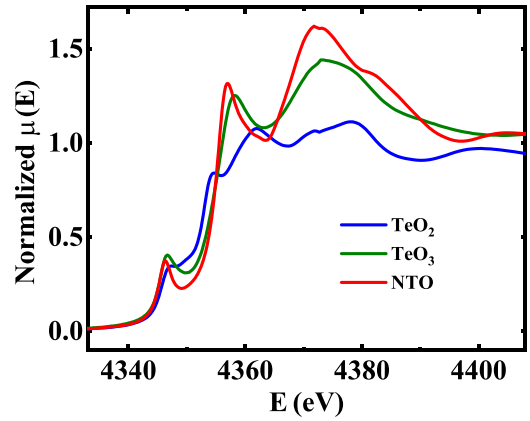

FIG. 5. Shows the Te-L_3 absorption edge measured at 300 K for NTO-air as well as the standard $TeO_2(Te^{4+})$ and $TeO_3(Te^{6+})$.

it resides at 2.3 eV lower and at 1 eV higher energies, respectively. This shift in the rising edge with oxidation state is expected and it is already discussed in connection with Ni^{2+} and Ni^{3+} states (see Sec. III C 1). The first derivative of the absorption coefficient at the rising edge also shows that the peak for NTO resides somewhat close to TeO_3 albeit a at slightly lower energy (~ 0.5 eV). It indicates that the majority of the Te ions are in the 6+ state, although certain fractions are also in the 4+ state.

D. X-ray photoelectron spectroscopy

To investigate the oxygen off-stoichiometry towards the mixed valency of Ni, we study three different batches of Ni_3TeO_6 samples, namely, NTO-air, NTO-vac, and NTO-oxy. The obtained data were calibrated using the standard carbon $1s$ peak located at 285.4 eV. Such vacuum and oxygen annealings are likely to change oxygen stoichiometry in Ni_3TeO_6. We recorded x-ray photoemission spectra of O-$1s$, Ni-$2p$, and Te-$3d$ levels for all three samples [see Figs. 6(a) to 6(i)]. The Ni-$2p$ spectra show two distinct set of peaks ($2p_{1/2}$ + satellite and $2p_{3/2}$ + satellite) originating from the spin-orbit interaction. The Ni-$2p_{3/2}$ shows a main peak at 855.1 eV along with a satellite line at 861.2 eV. For the Ni^{2+} state (as in NiO), the binding energy (BE) of the $2p_{3/2}$ level is about 854.5 eV [48,49]. This indicates that the BE of $2p_{3/2}$ in NTO is slightly higher than the pure 2+ state. This is possibly due to the presence of Ni in the higher oxidation state, which is also evident from our XANES study. We found that a single Lorentz convoluted Gaussian line did not fit the Ni-$2p_{3/2}$ spectra. Nevertheless, two Lorentz convoluted Gaussians provide a good fit to the data [Fig. 6(a)], and they correspond to two different charge states of Ni, namely, Ni^{2+} and Ni^{3+} with a ratio 1 : 0.49. Interestingly, there is practically no difference in peak position and the profile of the Ni-$2p_{3/2}$ lines in NTO-air, NTO-vac, and NTO-oxy indicating that annealing in different environments hardly changes the Ni charge state [Figs. 6(a) to 6(c)]. We also found some signatures of the mixed-valency of Ni ions in an air annealed sample previously [23].

The Te-$3d$ spectra for the NTO-air, NTO-vac, and NTO-oxy is depicted in Figs. 6(d) to 6(f). Similar to Ni peaks, the Te-$3d$ peaks are found to be identical in all three samples.

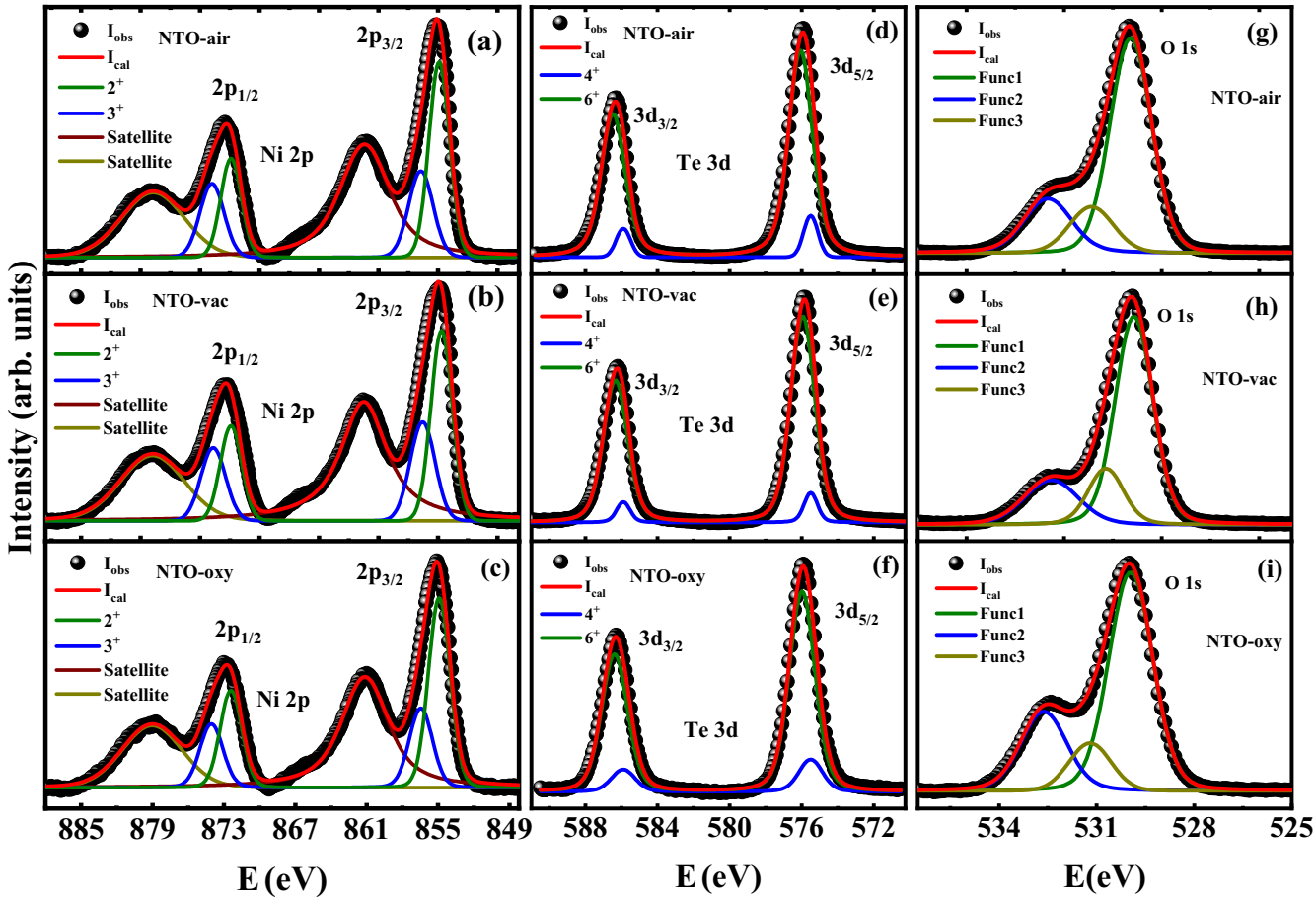

FIG. 6. (a)–(c) The Ni-2*p* x-ray photoemission peaks for the sample annealed in air, vacuum, and oxygen, respectively. The Te-3*d* peaks for different samples are shown in (d)–(f), while the O-1*s* peaks are depicted in (g)–(i).

The 3*d* line of Te is split into $3d_{3/2}$ and $3d_{5/2}$ due to spin-orbit coupling. The $3d_{5/2}$ line of NTO occurs at 575.9 eV, which is slightly lower than the BE of 576.4 eV reported for the Te^{6+} state (as in TeO_3) [50,51]. Such observation further indicates that Te is also in a mixed valent state similar to Ni. The O-1*s* line of the NTO sample is observed around 530 eV and there exists a shoulder-like feature around 532.5 eV [Fig. 6(g)]. The peak can be fitted with three Lorentz convoluted Gaussian singlets. The O-1*s* peaks of NTO-vac and NTO-oxy samples are found to be almost identical with that of NTO-air [Figs. 6(g) to 6(i)].

E. Extended x-ray absorption fine structure

To have precise information about the temperature evolution of the local structure of NTO, we analyzed the EXAFS part of the absorption data recorded between 300 and 20 K. Figure 7(a) shows the imaginary part and the modulus of the Fourier transform (|FT|) of the EXAFS signal of the data at 300 K compared with the best fit up to 3.5 Å. We used FEFF6 to calculate the phase shifts and effective scattering amplitudes of the atoms [52]. Since, Ni occupies three different Wyckoff 3*a* sites, we used an aggregate FEFF calculation. The scattering paths within 0.15 Å were merged together, and weighted by the fractional population of the site in the unit cell [53]. For our calculation, we only considered single scattering (SS) paths for the electrons. The k^3 weighted experimental spectra with the best fit along with different scattering paths are depicted in Fig. 7(b) and the partial contributions from different shells at different average distances are shown below for better visualization. The scattering amplitudes for different atoms are denoted by O SS 2.005, O SS 2.13,..., Ni SS 3.654, where the first letter/letters denote the symbol of the scattering atom, SS stands for single scattering, and the number denotes the distance from Ni atom (active site) to the scatterer. It is to be noted that the scattering paths at 3.622 Å and 3.654 Å are considered for a better fit to the data below 3.5 Å.

The temperature variations of the |FT| of the k^2 weighted experimental EXAFS data are shown in Fig. 7(c). There is a systematic increase in the amplitude of the |FT| data with the lowering of temperature, which is likely to be connected with the decrease of the Debye-Waller factor (DWF) with decreasing temperature. Additionally, there is a weak shift of the peak around 2.6 Å to higher values of R with the lowering of T. From our EXAFS analysis, we conclude that this peak primarily originate from adjacent Ni and Te atoms. Therefore, the anomaly may be attributed to the change in Ni-Ni and Ni-Te bond lengths with temperature. The DWF also increases with the increase in distance (R) from the Ni atom following the equation $I = I_0 \exp(-q^2 < u^2 > /3)$. The valley around

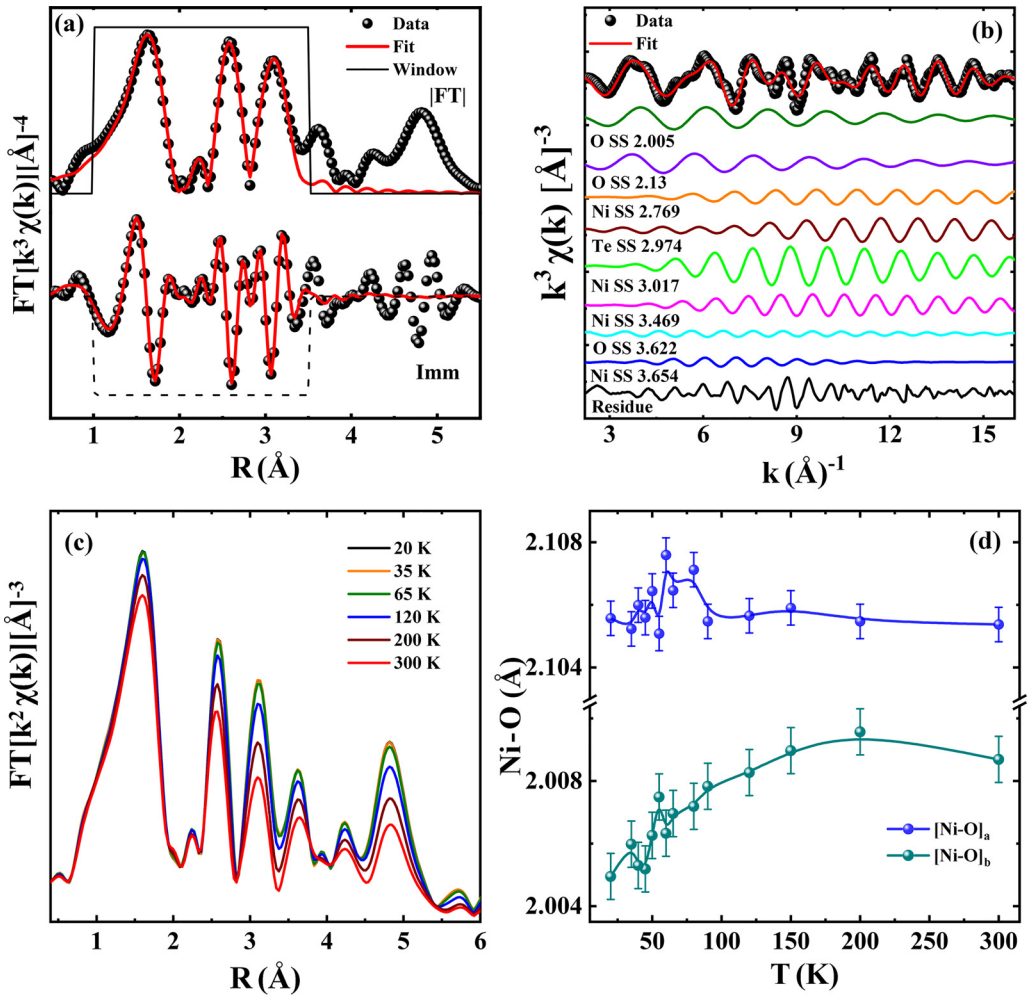

FIG. 7. (a) The Fourier transforms of the respective experimental data (black circles) and the theoretical fitted curve (solid red line); the magnitude (|FT|) and the imaginary parts (I_{mm}) are indicated and they are vertically shifted for clarity. (b) Ni-K edge k^3 weighted experimental EXAFS data (shaded black circles) at $T = 200$ K and the corresponding best fit (red solid line). Here O SS 2.005 represents the average distance of different oxygen from Ni within the aggregate resolution is 2.005 Å, and other notations also signify the usual meaning. (c) The temperature variation of the radial distribution function with R. The variation of the Ni-O bond lengths inside the $Ni-O_6$ octahedra with T are depicted in (d). The two different sets of oxygen inside three different $Ni-O_6$ octahedra are designated as $[Ni-O]_a$ and $[Ni-O]_b$, respectively.

2.8 Å represents the nonavailability of any significant scatterer at that distance from the Ni atom. The same is applicable for all other dips as all, however, the increase in the DWF with temperature and R makes them more prominent at higher values of R.

Figure 7(d) shows the temperature variation of the Ni-O bond length for two different oxygen sites. We find an anomaly in the data around T_N, which supports a similar feature observed in the lattice parameter [see Figs. 1(c) to 1(e)].

IV. DISCUSSION

Despite having noncentrosymmetric crystal structure, NTO does not show switchable spontaneous polarization down to 2 K. However, below the long-range antiferromagnetic transition at $T_N = 52$ K, the sample shows nonswitchable electric polarization (P) along with the colossal magnetoelectric effect. The compound has been referred to as a pyroelectric material. In the present work, we primarily addressed the thermal evolution of the sample from the crystallographic point of view.

An important outcome of our study is the presence of the lattice anomaly as evidenced from the analysis of our temperature-dependent PXRD and EXAFS data. As a consequence of the lattice anomaly, sharp discontinuity is also present in the lattice volume [see the inset of Fig. 1(a)] around T_N. Since volume is the first derivative of Gibb's free energy $V = (\frac{\partial G}{\partial P})_T$, a discontinuity in the lattice volume indicates the first-order nature of the transition. This is also supported by the anomaly in Ni-O bond distances in the NiO_6 octahedra close to T_N.

The essence of the lattice anomaly concomitant with the magnetic transition points towards the magnetostructural instability in the system, which was already conjectured in the previous works [16]. The lattice anomaly due to exchange striction occurs from the competition between magnetic and lattice energies, and the system stabilizes with an optimized

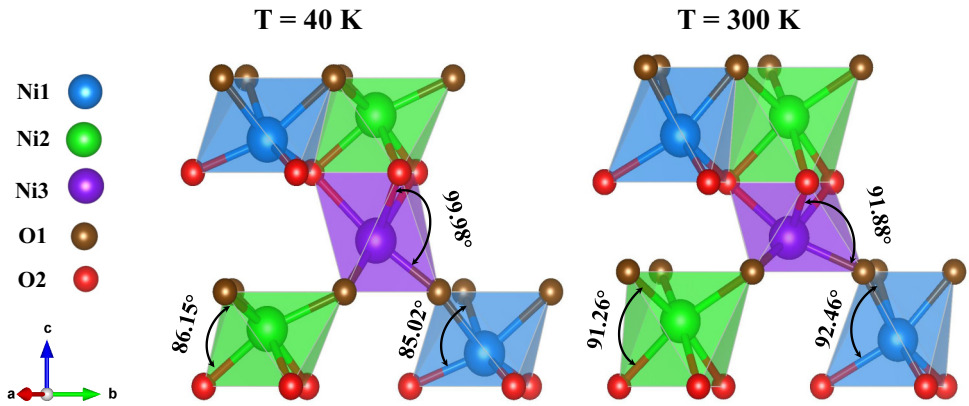

FIG. 8. Perspective views of the NiO_6 octahedra at 40 K and 300 K.

separation of magnetic ions. The application of the magnetic field can disrupt this equilibrium leading to further change in the ionic separation, which in its turn can induce the ME effect. It is to be noted that ∠[O-Ni-O] in the NiO_6 octahedra are close to 90° at 300 K. However, a larger deviation from 90° is observed in all ∠[O-Ni-O] at lower temperatures as shown in Fig. 8. This is due to the trigonal distortion in all three Ni-octahedra associated with the exchange striction.

Interestingly, our magnetic measurement indicates clear evidence for the thermal hysteresis around T_N. The hysteresis spans a wide temperature range. Previous works identified the magnetic transition to be second order in nature [16]. However, the presence of thermal hysteresis clearly rules out the possibility of a continuous transition in NTO [54].

The second most important point of the present study is the mixed valency of Ni and Te. In previous works till now, the oxidation states of Ni and Te were considered to be 2+ and 6+, respectively [55]. However, our XANES data indicate the presence of Ni^{3+} alongside Ni^{2+}. Similarly, a fraction of Te ions attains a 4+ state. This might happen due to charge disproportionation between Ni and Te ions, $Ni^{2+} + Te^{6+} \Longleftrightarrow Ni^{3+} + Te^{4+}$.

The value of the effective paramagnetic moment also supports the mixed valency in Ni. In the literature, there is a wide range of values of the reported Ni moment for NTO [17,22,56]. In most cases, the value of μ_{eff} is higher than the spin-only value (2.83 μ_B) of the Ni^{2+} moment. We carefully addressed the issue, and the value of μ_{eff} is found to be 3.32 μ_B/Ni for NTO-air. It is to be noted that the value of μ_{eff} for NTO-air is found to be almost same for NTO-vac and NTO-oxy.

However, one may argue that the orbital moment of Ni is not fully quenched in NTO, and one can get a higher value of the paramagnetic moment in the presence of spin-orbit coupling (SOC). Neutron diffraction study on the powdered samples indicates that the Ni spins are oriented along the c axis of the crystal [17]. The ground-state spin orientation of NTO was investigated by density functional theory (DFT) based calculation (GGA+ U + SOC) under the generalized gradient approximation (GGA), where both onsite Coulomb interaction (U) and SOC were taken into account [32]. The calculation indicates that the minimum energy state has moments perpendicular to the c axis, which simply contradicts the experimental observation. Nevertheless, a GGA + U calculation, where the SOC is excluded, reproduces the realistic result with moments parallel to the c axis. This indicates that SOC has no significant role in this compound, and Ni contributes the spin-only moment. So, the origin of the higher moment can be ascribed to Ni^{3+} ions, which is also supported by our XANES study.

Our XPS study on three different batches of samples (air, vacuum, and oxygen annealed, respectively) does not show any marked difference in the O, Ni, and Te peaks with annealing procedure. Neither do they show any significant difference in the values of μ_{eff} implying a stable charge state of Ni ions. This indicates that the compound is quite stable and its oxygen stoichiometry does not change much with the annealing procedure. It conveys that the mixed valency in NTO is robust and possibly intrinsic to the sample.

There are several examples in the literature [57–59], where multiferroicity or the ME effect is related to the mixed valency of the magnetic ions. For example, the mixed valent state of Mn and Fe are important for the magnetoelectric effect in $CaMn_7O_{12}$ and $CaBaFe_4O_7$, respectively. The orthorhombic mixed valent manganites RMn_2O_5 (R = rare-earth) also show giant ME effects, which are thought to arise from the parity-breaking Mn^{3+}-Mn^{4+} isotropic exchange interaction [11,57,58,60,61]. In the case of $CaMn_7O_{12}$, $CaBaFe_4O_7$, and RMn_2O_5, the mixed valency of the metal ions is site specific. However, for NTO, it is difficult to say whether Ni^{3+} or Ni^{2+} ions occupy definite crystallographic sites or they are randomly distributed in the lattice. Nevertheless, the mixed valency in NTO can be a possible route to the large ME effect observed in the compound.

In the XAS study, the Ni pre-edge in NTO is found to be more prominent than that of NiO. The pre-edge transition ($1s \rightarrow 3d$) is not dipole allowed and it primarily occurs due to the mixing of Ni-3d with Ni-4p or O-2p states [39,62,63]. In the case of octahedral distortion, the metal ion (here Ni) can lose the inversion symmetry. If the metal ion lacks the inversion symmetry, there will be mixing of the 3d and 4p levels [38]. The Ni-O bond lengths in the NiO_6 octahedra of NTO are different [see the values of O SS in Fig. 7(b)]

leading to distortion. This may result to greater *p-d* mixing and a stronger pre-edge.

Interestingly, the intensity of the pre-edge peak shows a distinct anomaly at the AFM ordering temperature. Such an anomaly can be attributed to the exchange-striction observed in our PXRD data [see Figs. 1(c) and 1(d)]. The Ni-O-Ni AFM superexchange mechanism can also have some effect on the transition probability associated with the pre-edge leading to the anomaly in the pre-edge peak area at T_N.

In conclusion, we performed a comprehensive analysis of the structural details of the magnetoelectric compound Ni_3TeO_6 through PXRD, XPS, and XAS studies. An isostructural instability is seen at the Néel temperature, which can be assigned to exchange-striction effect. The observed structural anomaly can be seen from the local probe such as EXAFS, and it is also evident in the overall change from our PXRD analysis. Our work also points out the mixed valence states of cations, which is presumably related to the charge disproportionation between Ni and Te ions. The mixed valency of Ni is also evident in the paramagnetic moment of the sample as obtained from our magnetization measurements. Such charge disproportionation can be instrumental in the observed magnetic and electric anomalies in Ni_3TeO_6.

ACKNOWLEDGMENTS

MN would like to thank CSIR, India for his research fellowship [File No. 09/080(1131)/2019-EMR-I]. The Department of Science and Technology (India) is acknowledged for financial support (KEK Proposal No. 2021-IB-32), and the Saha Institute of Nuclear Physics and Jawaharlal Nehru Centre for Advanced Scientific Research, India for facilitating the experiments at the Indian Beam Line, Photon Factory, KEK, Japan. We also acknowledge Elettra Sincrotrone Trieste for providing access to its synchrotron radiation facilities with XAFS beamline (Proposal No. 20210469).

[1] N. A. Spaldin and M. Fiebig, Science **309**, 391 (2005).
[2] S.-W. Cheong and M. Mostovoy, Nat. Mater. **6**, 13 (2007).
[3] D. Khomskii, Physics **2**, 20 (2009).
[4] Y. Tokura, S. Seki, and N. Nagaosa, Rep. Prog. Phys. **77**, 076501 (2014).
[5] W. Eerenstein, N. D. Mathur, and J. F. Scott, Nature (London) **442**, 759 (2006).
[6] Y. Tokunaga, N. Furukawa, H. Sakai, Y. Taguchi, T.-H. Arima, and Y. Tokura, Nat. Mater. **8**, 558 (2009).
[7] Y. Tokunaga, Y. Taguchi, T.-H. Arima, and Y. Tokura, Nat. Phys. **8**, 838 (2012).
[8] T. Lottermoser, T. Lonkai, U. Amann, D. Hohlwein, J. Ihringer, and M. Fiebig, Nature (London) **430**, 541 (2004).
[9] H. Katsura, N. Nagaosa, and A. V. Balatsky, Phys. Rev. Lett. **95**, 057205 (2005).
[10] I. A. Sergienko and E. Dagotto, Phys. Rev. B **73**, 094434 (2006).
[11] L. C. Chapon, G. R. Blake, M. J. Gutmann, S. Park, N. Hur, P. G. Radaelli, and S.-W. Cheong, Phys. Rev. Lett. **93**, 177402 (2004).
[12] C. Jia, S. Onoda, N. Nagaosa, and J. H. Han, Phys. Rev. B **74**, 224444 (2006).
[13] C. Jia, S. Onoda, N. Nagaosa, and J. H. Han, Phys. Rev. B **76**, 144424 (2007).
[14] T.-H. Arima, J. Phys. Soc. Jpn. **76**, 073702 (2007).
[15] X. Z. Lu, M.-H. Whangbo, S. Dong, X. G. Gong, and H. J. Xiang, Phys. Rev. Lett. **108**, 187204 (2012).
[16] Y. S. Oh, S. Artyukhin, J. J. Yang, V. Zapf, J. W. Kim, D. Vanderbilt, and S.-W. Cheong, Nat. Commun. **5**, 3201 (2014).
[17] I. Živković, K. Prša, O. Zaharko, and H. Berger, J. Phys.: Condens. Matter **22**, 056002 (2010).
[18] J. Lass, C. R. Andersen, H. K. Leerberg, S. Birkemose, S. Toth, U. Stuhr, M. Bartkowiak, C. Niedermayer, Z. Lu, R. Toft-Petersen, M. Retuerto, J. O. Birk, and K. Lefmann, Phys. Rev. B **101**, 054415 (2020).
[19] J. W. Kim, S. Artyukhin, E. D. Mun, M. Jaime, N. Harrison, A. Hansen, J. J. Yang, Y. S. Oh, D. Vanderbilt, V. S. Zapf, and S.-W. Cheong, Phys. Rev. Lett. **115**, 137201 (2015).
[20] M. O. Yokosuk, S. Artyukhin, A. al Wahish, X. Wang, J. Yang, Z. Li, S.-W. Cheong, D. Vanderbilt, and J. L. Musfeldt, Phys. Rev. B **92**, 144305 (2015).
[21] M. Lines, Solid State Commun. **11**, 1615 (1972).
[22] R. Sankar, G. J. Shu, B. Karunakara Moorthy, R. Jayavel, and F. C. Chou, Dalton Trans. **42**, 10439 (2013).
[23] M. Numan, M. Salman Khan, and S. Majumdar, Mater. Today: Proc. **57**, 151 (2022).
[24] For the preparation of NTO-oxy, TeO_3 was prepared by heating H_6TeO_6 at 350° C for 4 h. Then the stoichiometric amount of NiO and the as prepared TeO_3 were mixed and grounded thoroughly and heated at 750° C for 10 h under constant oxygen flow. After that, the same heat treatment was followed as NTO-air except that this time the heating was done under continuous oxygen flow
[25] http://maud.radiographema.eu/.
[26] A. D. Cicco, G. Aquilanti, M. Minicucci, E. Principi, N. Novello, A. Cognigni, and L. Olivi, J. Phys.: Conf. Ser. **190**, 012043 (2009).
[27] M. Newville, J. Synchrotron Radiat. **8**, 322 (2001).
[28] B. Ravel and M. Newville, J. Synchrotron Radiat. **12**, 537 (2005).
[29] X. Torrelles, G. Cantele, G. M. De Luca, R. Di Capua, J. Drnec, R. Felici, D. Ninno, G. Herranz, and M. Salluzzo, Phys. Rev. B **99**, 205421 (2019).
[30] L. Hu, C. Xie, S. J. Zhu, M. Zhu, R. H. Wei, X. W. Tang, W. J. Lu, W. H. Song, J. M. Dai, R. R. Zhang, C. J. Zhang, X. B. Zhu, and Y. P. Sun, Phys. Rev. B **103**, 085119 (2021).
[31] S. Landron and M.-B. Lepetit, Phys. Rev. B **77**, 125106 (2008).
[32] F. Wu, E. Kan, C. Tian, and M.-H. Whangbo, Inorg. Chem. **49**, 7545 (2010).
[33] J. B. Goodenough, Phys. Rev. **100**, 564 (1955).
[34] J. B. Goodenough, J. Phys. Chem. Solids **6**, 287 (1958).
[35] J. Kanamori, J. Phys. Chem. Solids **10**, 87 (1959).
[36] G. Subías, J. Blasco, S. Lafuerza, V. Cuartero, M. C. Sánchez, R. Boada, S. Díaz-Moreno, F. Fauth, and J. García, Inorg. Chem. **59**, 15757 (2020).

[37] W. Xie, Y.-L. Lee, Y. Shao-Horn, and D. Morgan, J. Phys. Chem. Lett. **7**, 1939 (2016).
[38] F. Bridges, C. H. Booth, M. Anderson, G. H. Kwei, J. J. Neumeier, J. Snyder, J. Mitchell, J. S. Gardner, and E. Brosha, Phys. Rev. B **63**, 214405 (2001).
[39] M. C. Sánchez, J. García, J. Blasco, G. Subías, and J. Perez-Cacho, Phys. Rev. B **65**, 144409 (2002).
[40] O. Durmeyer, E. Beaurepaire, J.-P. Kappler, C. Brouder, and F. Baudelet, J. Phys.: Condens. Matter **22**, 125504 (2010).
[41] A. Yoshiasa, G. Kitahara, T. Tobase, T. Hiratoko, H. Hongu, T. Nakatani, and K.-I. Murai, Phys. Status Solidi (B) **255**, 1800050 (2018).
[42] J. Wong, F. W. Lytle, R. P. Messmer, and D. H. Maylotte, Phys. Rev. B **30**, 5596 (1984).
[43] I. J. Pickering, G. N. George, J. T. Lewandowski, and A. J. Jacobson, J. Am. Chem. Soc. **115**, 4137 (1993).
[44] P. Aich, C. Meneghini, and S. Ray, Mater. Res. Express **6**, 026103 (2018).
[45] H. Singh, A. K. Sinha, S. M. Gupta, M. N. Singh, and H. Ghosh, J. Am. Ceram. Soc. **99**, 3443 (2016).
[46] A. Waehayee, N. Chanlek, P. Kidkhunthod, H. Nakajima, S. Suthirakun, and T. Siritanon, Phys. Rev. B **100**, 045132 (2019).
[47] A. Berthereau, E. Fargin, A. Villezusanne, R. Olazcuaga, G. Le Flem, and L. Ducasse, J. Solid State Chem. **126**, 143 (1996).
[48] K. Kim and N. Winograd, Surf. Sci. **43**, 625 (1974).
[49] P. Lorenz, J. Finster, G. Wendt, J. Salyn, E. Žumadilov, and V. Nefedov, J. Electron Spectrosc. Relat. Phenom. **16**, 267 (1979).
[50] J. Wang, J. A. C. Santana, N. Wu, C. Karunakaran, J. Wang, P. A. Dowben, and C. Binek, J. Phys.: Condens. Matter **26**, 055012 (2014).
[51] P. Pal, A. Sahoo, M. F. Abdullah, S. D. Kaushik, P. N. Vishwakarma, and A. K. Singh, J. Appl. Phys. **124**, 164110 (2018).
[52] M. Newville, J. Synchrotron Radiat. **8**, 96 (2001).
[53] B. Ravel, J. Synchrotron Radiat. **21**, 1269 (2014).
[54] P. M. Chaikin and T. C. Lubensky, *Principles of Condensed Matter Physics* (Cambridge University Press, Cambridge, England, 1995).
[55] A. Ghosh, K.-H. Chen, X.-S. Qiu, S. H. Hsieh, Y. C. Shao, C. H. Du, H. T. Wang, Y. Y. Chin, J. W. Chiou, S. C. Ray, H. M. Tsai, C. W. Pao, H. J. Lin, J. F. Lee, R. Sankar, F. C. Chou, and W. F. Pong, Sci. Rep. **8**, 15779 (2018).
[56] I. Panneer Muthuselvam, K. Saranya, R. Sankar, R. N. Bhowmik, and L. Kavitha, J. Appl. Phys. **128**, 123902 (2020).
[57] V. Kocsis, Y. Tokunaga, S. Bordács, M. Kriener, A. Puri, U. Zeitler, Y. Taguchi, Y. Tokura, and I. Kézsmárki, Phys. Rev. B **93**, 014444 (2016).
[58] J. Sannigrahi, S. Chattopadhyay, D. Dutta, S. Giri, and S. Majumdar, J. Phys.: Condens. Matter **25**, 246001 (2013).
[59] V. A. Stephanovich, M. D. Glinchuk, and R. Blinc, Europhys. Lett. **83**, 37004 (2008).
[60] L. C. Chapon, P. G. Radaelli, G. R. Blake, S. Park, and S.-W. Cheong, Phys. Rev. Lett. **96**, 097601 (2006).
[61] G. R. Blake, L. C. Chapon, P. G. Radaelli, S. Park, N. Hur, S.-W. Cheong, and J. Rodríguez-Carvajal, Phys. Rev. B **71**, 214402 (2005).
[62] M. Mizumaki, N. Ishimatsu, N. Kawamura, M. Azuma, Y. Shimakawa, M. Takano, and T. Uozumi, Phys. Rev. B **80**, 233104 (2009).
[63] A. Y. Ramos, C. Piamonteze, H. C. N. Tolentino, N. M. Souza-Neto, O. Bunau, Y. Joly, S. Grenier, J.-P. Itié, N. E. Massa, J. A. Alonso, and M. J. Martinez-Lope, Phys. Rev. B **85**, 045102 (2012).